

3D numerical study on microwave induced stresses in inhomogeneous hard rocks

Michael Toifl ^{a,b,*}, Ronald Meisels ^{a,c}, Philipp Hartlieb ^{a,d}, Friedemar Kuchar ^{a,c}, Thomas Antretter ^{a,b}

^a Montanuniversitaet Leoben, Franz-Josef-Strasse 18, 8700 Leoben, Austria

^b Institute of Mechanics, Austria

^c Institute of Physics, Austria

^d Chair of Mining Engineering and Mineral Economics, Austria



ARTICLE INFO

Article history:

Received 29 June 2015

Revised 3 December 2015

Accepted 10 January 2016

Available online 18 January 2016

Keywords:

Microwave heating

Thermally induced stresses

3D artificial microstructure

Quartz phase transformation

FDTD–FEM

ABSTRACT

The aim of this research is to present a novel 3D simulation procedure to assess microwave induced stresses in inhomogeneous hard rocks at a microstructure level. For a realistic rock model a two-component 3D microstructure is generated by a Voronoi tessellation algorithm. The two components are microwave absorbing (phase A) and transparent (phase T), respectively. In order to calculate the electric field inside the inhomogeneous rock, a 3D finite difference time domain (FDTD) simulation is performed. The absorbed heat is computed and applied as temperature distribution in a subsequent thermo-mechanical finite element (FE) analysis in order to calculate the thermally induced stresses. Two irradiation times (15 s and 25 s) and a microwave power of 25 kW at 2.45 GHz as well as three different morphologies are analyzed. Moreover, the phase transformation of quartz at 573 °C is considered in the FE model. The influence of the anisotropic nature of the quartz grains is assessed by comparing the stress formation in the isotropic with those of the anisotropic case. A comparative analysis with a homogeneous model is performed in order to draw conclusions on the influence of the microstructure on the microwave induced stress formation. High maximum principal stresses on the boundaries of the microwave absorbing phase (phase A) exceeding the tensile strength are observed in the 15 s irradiation model. After 25 s of microwave irradiation even higher stresses as a consequence of phase transformation of quartz are determined. In the anisotropic case significantly more areas with high maximum principal stresses especially in phase T are observed. Microwave irradiation experiments on granite samples are performed in order to correlate the numerical results with experiments.

© 2016 The Authors. Published by Elsevier Ltd. This is an open access article under the CC BY license (<http://creativecommons.org/licenses/by/4.0/>).

1. Introduction

Classical mechanical comminution is a highly energy-intensive process which consumes up to 2% of the total energy in several mining countries such as USA, Australia and South Africa (Tromans, 2008). However, less than 1% of this energy is actually used to generate new surfaces (DOE, 2007; Fuerstenau and Abouzeid, 2002). In other words, almost the complete energy provided for the process is dissipated in the form of heat and noise. High energy and maintenance cost as well as strict sustainability regulations call for more efficient mining processes. A highly promising technique, which has the potential to significantly increase the efficiency, is the preceding microwave treatment of rocks followed by mechanical breakage operations. The aim of

the microwave irradiation is to pre-damage the rock (cracks, spallation) in order to weaken its mechanical properties. Microwave heating is driven by the absorption of microwave energy by the rock combined with the conversion of the electromagnetic energy into heat. Therefore, temperature gradients are introduced into the rock that generate thermally induced stresses which can exceed the strength of the rock.

The physical process of microwave heating is described by the complex dielectric constant ϵ (permittivity): $\epsilon = \epsilon_r + i\epsilon_i = \epsilon_0(\kappa_r + i\kappa_i)$. κ_r is the real part of the relative permittivity, κ_i the imaginary part and ϵ_0 defines the permittivity of vacuum. The absorption of microwaves is mainly governed by κ_i . According to Santamarina (1989) typical values for hard rocks range from 10^{-3} – 50 for κ_i and 2 – 10 for κ_r depending on frequency and temperature. Since rocks contain several minerals arranged in various distributions, different κ_i values appear in the material. Microwave absorbing minerals are plagioclase ($\kappa_i = 0.004$ – 0.32 [Kržmanc et al., 2003;

* Corresponding author at: Montanuniversitaet Leoben, Franz-Josef-Strasse 18, 8700 Leoben, Austria.

E-mail address: michael.toifl@unileoben.ac.at (M. Toifl).

Zheng et al., 2005]), pyroxene ($\kappa_i = 1.62$ [Zheng et al., 2005]) and ilmenite ($\kappa_i = 32.58$ [Zheng et al., 2005]) whereas quartz ($\kappa_i = 0.0006\text{--}0.0033$ [Webb and Church, 1986; Zheng et al., 2005]), orthoclase ($\kappa_i = 0.00019$ [Church et al., 1988]) and muscovite ($\kappa_i = 0.0006\text{--}0.0034$ [Webb and Church, 1986; Church et al., 1988]) are poorly absorbing. Consequently, an inhomogeneous thermal field is expected. Recently, several numerical studies of rocks with heterogeneous microstructures showed that the resulting stresses are high enough to initiate cracks around phase boundaries of high-absorbing particles which can propagate further into the material (Ali and Bradshaw, 2010, 2011; Jones et al., 2005; Meisels et al., 2015; Toifl et al., 2014; Wang et al., 2008; Wang and Djordjevic, 2014). However, in these studies no realistic microstructures were considered and furthermore only 2D models were used. Fitzgibbon and Veasey (1990) concluded that these thermally induced cracks may lead to a significant reduction in grinding resistance during comminution processes.

The main advantage of using microwave heating of inhomogeneous hard rocks is that only the high-absorbing minerals are affected and therefore selective heating occurs. However, experiments on rather homogeneous rocks such as basalt also show significant microwave induced damage without any high absorbing particles (Hartlieb et al., 2012; Peinsitt et al., 2010; Satish et al., 2006). There the thermal gradients between the homogeneously heated area and the remaining bulk material and the heat loss at the free surfaces lead to high stresses. Although many promising experiments and numerical studies on the microwave induced damage of inhomogeneous rocks have already been performed, neither large-scale application nor commercial equipment exists. In our opinion this is due to the lack of understanding of the microwave induced damage on the microstructure level. In order to analyze the stress formation in heterogeneous rocks in detail, a realistic three-dimensional microstructure has to be built for the numerical calculations. Furthermore, different grains of various shapes and compositions should be investigated regarding their influence on the microwave induced damage.

The goal of the current research is to present a novel 3D simulation procedure in order to determine microwave induced stresses at a microstructure level and further to apply the proposed analysis on a hard rock model. Due to the lack of extensive thermo-physical measurements of different minerals occurring in hard rocks, a two phase model with data from literature was built up. The two components are microwave absorbing (phase A) and transparent (phase T), respectively. For a real rock phase T might be quartz and phase A a mixture of plagioclase, pyroxene and ilmenite. The dielectric properties of the two phases are derived from the

effective medium theory (Bruggeman, 1935) by taking an effective permittivity for hard rocks from literature. This theory might have its drawbacks but it has nevertheless been multiply verified and hence frequently been used in the literature to calculate the effective permittivity (Ciuchi et al., 2013; Kärkkäinen et al., 2000; Lou et al., 1997; Sihvola, 1989; Zhou et al., 2012).

In order to identify microwave induced stresses, a simulation chain is set up starting from the numerical solution of Maxwell's equations by means of a finite difference scheme (FDTD – finite difference time domain, see Tafløe (1995) and Yee (1966)) and a subsequent thermo-mechanical finite element (FE) analysis. The stress field of the 3D inhomogeneous microstructure model is compared with a model with homogeneous material definition. This allows drawing conclusions on the influence of the microstructural details. Moreover, two different irradiation times and the effect of the anisotropic behavior of the quartz grains (phase T) on the microwave induced stress are investigated. The analysis of a realistic 3D microstructure, including anisotropic material behavior as well as phase transformation with the goal of computing microwave induced stresses has, to the authors' knowledge, not yet been reported in the literature.

2. Methodology

Calculating the stress state inside a realistic 3D microstructure requires a comprehensive simulation methodology connecting different simulation modules. This work presents a simulation chain, for the time being without taking into account any feedback of temperature changes on the electromagnetic properties as well as a weak coupling between the displacements and the thermal field (Fig. 1).

The simulation process starts with the collection and pre-processing of input data such as physical and thermo-mechanical material properties, numerical parameters and model dimensions (Fig. 1). In the first numerical working package the 3D microstructure composed of polyhedra (=grains), is generated by a Voronoi tessellation algorithm (Quey et al., 2011). Within the next step the various grains are assigned to different phases according to a given random distribution function. In the current study a two component microstructure with a constant filling factor is assumed. This artificial microstructure represents the basic input for all further simulation modules. After that, the electric field inside the model rock is calculated by solving Maxwell's equations numerically applying a 3D FDTD (Finite Difference Time Domain) analysis (Tafløe, 1995; Yee, 1966). There the time averaged squared electric field E^2 is determined, which is used to derive

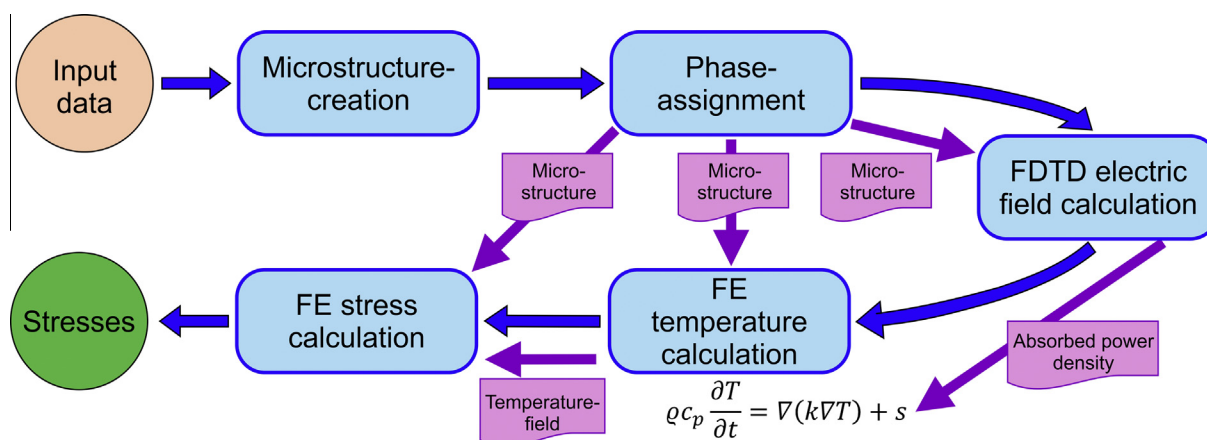


Fig. 1. Simulation chain, blue¹ arrows indicating sequential working path and purple arrows file transfers.

the absorbed power density distribution as the output of this module. In the subsequent thermal FE (Finite Element) simulation, the absorbed power density is directly treated as heat source entering the heat conduction equation which is solved numerically (Fig. 1). Therefore, a microwave irradiation time of 15 s (25 s in the model including phase transformation) with a microwave power of 25 kW followed by a cooling step of 3600 s is assumed. The transient inhomogeneous temperature field is used as an input for the FE stress simulation. Finally, the stress formation is analyzed in a statistical manner in order to predict the stress and hence damage formation in rock materials.

2.1. Microstructure

As mentioned above a Voronoi tessellation algorithm with statistical distributed grain size combined with phase assignment according to a constant filling factor is used. However, a more realistic phase distribution could be achieved in future works by considering spatial correlation in the microstructure model as presented by Tang et al. (2014). They built a similar unit cell taking into account a more realistic grain size and phase distribution as it may be observed in a microstructure analysis for mechanical fragmentation simulations. To this end they used a voxel based model. In the manuscript at hand, however, it was considered necessary to be able to capture the nature of the sharp grain boundaries, for that reason a Voronoi tessellation algorithm was preferred.

First, a cube is partitioned into polyhedra representing the grains of the material by a Voronoi tessellation algorithm provided by the open source software Neper (Quey et al., 2011). After that

the software performs some optimization loops (3 in the current case) in order to remove short edges of the polyhedra which would cause meshing problems. Subsequently, the grains are meshed with linear tetrahedral finite elements. At this point it is crucial that the desired amount of elements per polyhedron is set to values above 100, otherwise the meshing algorithm becomes highly constrained and would result in a low quality of the FE mesh. Unfortunately, the meshing process of the polyhedra is very time consuming and the time effort strongly increases with the amount of polyhedra. Here a microstructure of 30,000 grains is assumed which leads to manageable tessellation/meshing times and number of finite elements (4,060,685), see Fig. 2.

In the next step the material phases (phase A and T) are assigned to the different grains of the microstructure by a C++ script (Fig. 2). For the two component microstructure model, a filling factor f of 0.34 (volume of phase A in reference to total volume) is assumed. In the present paper three different morphologies with the same filling factor ($f = 0.34$) are investigated. In order to ensure a realistic grain size and to use the same tessellation for different grain diameters a finely meshed cube is embedded in a surrounding homogenized bulk material with averaged material properties (Fig. 3). The scaling of the cube depends on the desired average grain diameter, which is set to 3.2 mm in this work. This leads to a cube with an edge length of 8 cm containing the highly resolved microstructure. Moreover, the cube's edge length also results from the fact that at a distance of about 8 cm the temperature field has sufficiently decayed so that almost constant conditions can be assumed. From there on it is admissible to set the boundaries of the microstructure domain, respectively. A quarter symmetry of the whole numerical model is

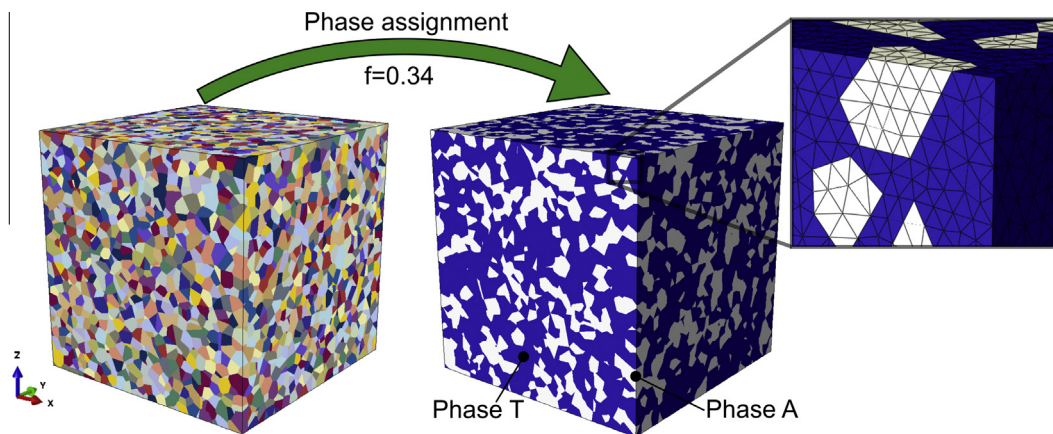


Fig. 2. Microstructure model and phase assignment of the various grains. Upper right close-up shows the FE mesh.

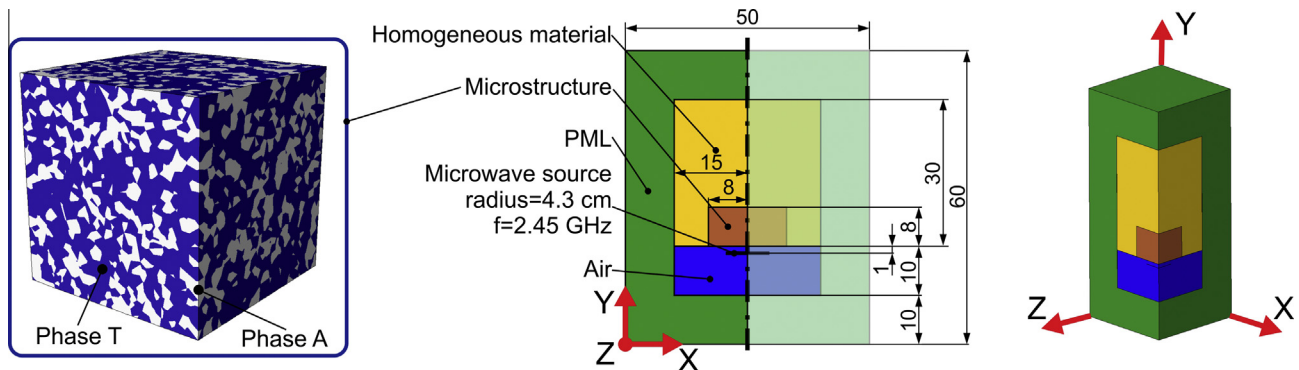


Fig. 3. Microstructure (left) and FDTD model (right, all dimensions in centimeters) including isometric view. PML stands for perfectly matched layer and is used to truncate the simulation model without causing reflections of the microwave.

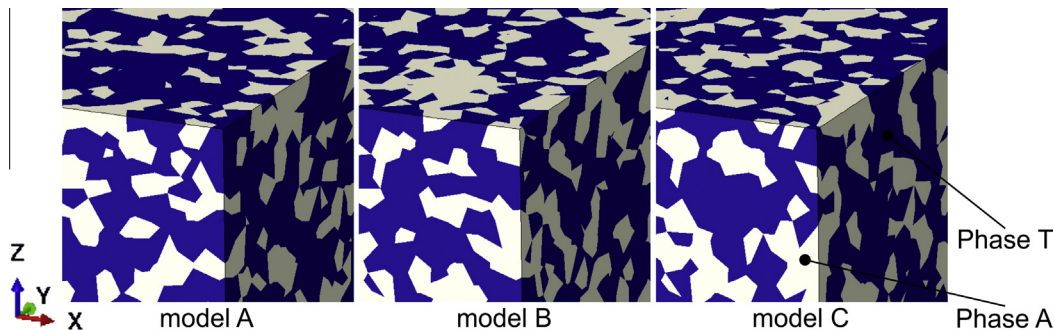


Fig. 4. Different models with same filling factor but different morphologies.

assumed in order to reduce the problem size and thus avoid excessive simulation times (Fig. 3). The material data of the homogeneous material is obtained by a linear mixture rule taking the two phases and the filling factor ($f = 0.34$) into account.

In order to assess different morphologies (different phase assignments) with the same filling factor f , two additional models with $f = 0.34$ are generated. The new models (model B and C) are compared with the reference model (model A) in Fig. 4.

Significant variations in the phase distribution are visualized in Fig. 4. In Section 3.3.4 the influence of the different morphologies on the microwave induced stresses is investigated.

2.2. FDTD Model

An FDTD algorithm explicitly solves Maxwell's equations describing the evolution of the electric field. A second order accurate central-difference approximation for space and time derivatives in the curl equations is applied (Taflove, 1988). In the current research the FDTD open source software MEEP (Oskooi et al., 2010) is used. The advantage of this software is the support of parallel computing, which is crucial to calculate the electric field in a sophisticated 3D model. In our case the FDTD simulations on a 12 core node with 256 Gb RAM took about 12 h. On top of that it is possible to link the program with C++ and therefore use object-oriented programming as well as all C++ libraries to define the material distribution according to the microstructure model defined in Section 2.1.

In Fig. 3 the whole FDTD model ($50 \times 60 \times 50 \text{ cm}^3$) is visualized. In addition to the quarter rock model (microstructure cube plus homogeneous material) described above, the model also includes air in front of the material as well as perfectly matched layers (PML) at the domain limits. The PML acts as a perfectly absorbing boundary which allows to truncate the simulation space without causing reflections of the electric field (Oskooi and Johnson, 2011). The thickness of the layer is chosen to be of the magnitude of the wavelength of the electric field. In the air the wavelength of a beam with a frequency of 2.45 GHz is $\lambda_{\text{air}} = 12 \text{ cm}$ and in the material ($\kappa_{\text{eff}} = 7.37 + 0.90i$) $\lambda_{\text{material}} = 4.5 \text{ cm}$. Since most of the PML is located around the material phase, a thickness of 10 cm is chosen and verified to be sufficient by various numerical simulations.

A microwave beam with a typical technical frequency of 2.45 GHz is applied. The shape of the beam is Gaussian (Kogelnik and Li, 1966) with a radius of 4.3 cm which corresponds to an opening of a waveguide at 2.45 GHz. It can be assumed that the Gaussian beam describes a planar wave (Jackson, 2011) at the source position which is parallel to the xz plane. The source plane is positioned 1 cm in front of the rock model and emits a beam which propagates in positive y-direction, whereas it is polarized in z-direction. A time and component averaged squared electric field value (E^2) of $1 \text{ V}^2/\text{m}^2$ is assumed at the middle axis of the

Gaussian beam (at $x = z = 25 \text{ cm}$ and $y = 19 \text{ cm}$). Since soft sources are used in MEEP, the equivalent electric and magnetic currents – representing the source – are derived based on the total-field/scattered-field approach (Taflove et al., 2013).

Since the dielectric constants of the various minerals vary strongly, depending on the experimental setup, water content and purity, an effective medium approach was chosen. The complex relative permittivity of the two phases of the model rock is calculated by assuming an effective permittivity κ_{eff} of the bulk material of $7.37 + 0.90i$, which is an upper limit of hard rocks for frequencies around 3 GHz (Santamarina, 1989). Phase T is assumed as microwave transparent (imaginary part of permittivity is zero) and phase A as microwave absorbing (imaginary part of permittivity is uneven zero). In order to increase the reflections at the interfaces between the transparent (phase T) and the absorbing (phase A) grains, which represents an upper limit case, a large difference between the real part of phase T ($\kappa_{T,r}$) and phase A ($\kappa_{A,r}$) is assumed. Therefore $\kappa_{T,r}$ is set to 7.1 and the remaining relative permittivity of phase A is derived by Bruggeman's effective medium theory (Bruggeman, 1935), see Eq. (1).

$$\kappa_A = \frac{(2 - 3f)\kappa_T - 2\kappa_{\text{eff}}}{(1 - 3f)\kappa_{\text{eff}} - \kappa_T} \kappa_{\text{eff}} \quad (1)$$

In Eq. (1), f describes the filling factor defined in Section 2.1. Applying Bruggeman's theory and the assumption made for κ_T the relative permittivity of the absorbing phase A, κ_A results in a value of $7.690 + 2.787i$. The high imaginary part of κ_A is explained by a mixture of strong absorbing minerals (pyroxene and ilmenite) with plagioclase representing the absorbing phase A.

Since the FDTD code is using an explicit solution scheme a stability condition has to be fulfilled (Eq. (2)). In Eq. (2), S stands for the Courant number, c for the velocity of light in vacuum, Δx for the lattice constant ($\Delta x = \Delta y = \Delta z$), n_{\min} for the minimum refractive index in the model and #dimension for the number of dimensions (Taflove, 1995).

$$S = \frac{c\Delta t}{\Delta x} < \frac{n_{\min}}{\sqrt{\# \text{ dimension}}} \quad (2)$$

Usually, a Courant number of 0.5 is chosen for 3D simulations. For avoiding numerical dispersion the lattice constant should be smaller than the wavelength divided by 20 (Taflove, 1988). In a parametric analysis the influence of the grid constant on the accuracy of the resulting thermal field combined with the computation effort has been investigated and a grid constant $\Delta x = \Delta y = \Delta z$ of 1 mm has been derived as the most appropriate value for the current models.

2.3. FE Model

A 3D finite element model has been developed using the FE package Abaqus (Abaqus, 2012). The size of the model equals the quarter model rock visualized in Fig. 5 (e.g. Fig. 3: homogeneous material plus microstructure). The cube containing the microstructure has already been meshed by the open-source program Neper (Quay et al., 2011) and in the homogeneous part a global element size ranging from 0.25 cm up to 1 cm is assumed which leads to 281,988 linear hexahedron elements. The entire model contains 4,342,673 elements and 1,000,173 nodes.

The two domains (microstructure cube and homogeneous part) are joined together by means of tie constraints of the respective surfaces. The thermo-mechanical material properties including the phase transformation of quartz are taken from the literature and are discussed in detail in Section 2.4. In the anisotropic model (anisotropic thermal conductance, thermal expansion and elastic constants), the local Cartesian coordinate system of each quartz grain (phase T) is randomly defined. Since no feedback of the displacement field on the heat flux is assumed, the thermo-mechanical simulation is divided in an uncoupled manner into a heat transfer and a subsequent stress analysis (Abaqus, 2012).

In the heat transfer model the Cartesian coordinates of the integration points of every finite element are read out by a FORTRAN subroutine. Afterwards, the absorbed power density ($\omega_e E^2$) is determined at each integration point (4 integration points in each tetrahedral finite element and 8 in each hexahedron element) by trilinear interpolation of the Euclidean norm of the time averaged squared electric field (E^2 , see Section 2.2). The source term of the heat conduction equation (body heat flux) is calculated by multiplying the absorbed power density with a constant. The constant factor is derived in an iterative manner by evaluating the energy balance of the thermal model, assuring that the total thermal energy within the rock model does not exceed the energy input by the microwave source (25 kW minus 30% of losses, which was evaluated by various experimental investigations). The losses account for the reflections inside the waveguide and the imperfect formation of the Gaussian beam. The body heat flux is applied in each increment of the thermal analysis at the respective integration point by a DFLUX subroutine (Abaqus, 2012). On the front face of the material model (blue¹ dashed-dotted line in Fig. 5) a thermal conductance of 20 W/m² K and heat transfer coefficient of 0.8 combined with an ambient temperature of 25 °C is assumed. At all other faces, i.e., the cutting planes where the model is truncated, a heat transfer coefficient of 0.8 is assumed. At the beginning of the thermal analysis all nodes are set to 25 °C. The model is heated for 15 s or 25 s, respectively, and then it naturally cools down (i.e. the body heat flux is switched off) for 3600 s. The thermal model has 1,875,188 degrees of freedom.

In the mechanical model the same FE mesh again using linear elements as in the thermal analysis is employed. Furthermore the same two steps (heating and cooling) are analyzed. The mechanical model has 3,000,519 degrees of freedom. As an input the time varying temperature field calculated in the previous analysis is applied. On the xy cutting plane (Fig. 5) of the quarter model the displacements in z direction, and on the yz plane (red dashed line in Fig. 5) the displacements in x directions are set to zero as the symmetric boundary conditions for the stress calculation. Moreover, the node located at the Gaussian axis on the front face of the model is fixed in y-direction. An elastic material behavior is assumed for all constituents (see Section 2.4).

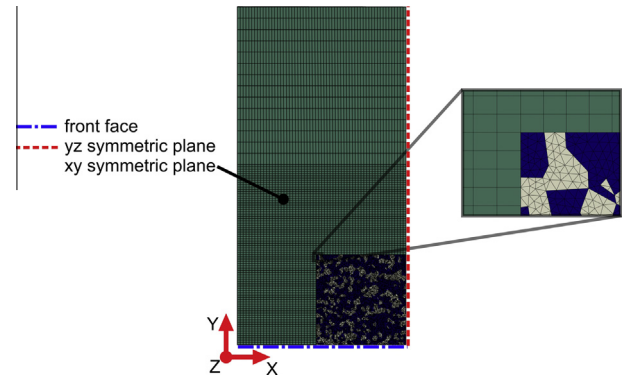


Fig. 5. FE mesh with linear tetrahedron and hexahedron elements.

The presented methodology is limited to temperature independent dielectric properties since no strong coupling between FDTD – and FE simulation is considered. Future work will also include this effect in a more sophisticated simulation procedure.

2.4. Thermo-mechanical material properties

Unlike the permittivity, the thermo-mechanical properties of minerals are well known in literature. Therefore the main constituent of phase A and of phase T is chosen for the FE simulations. In the paper at hand, quartz represents the microwave transparent phase T and plagioclase as the main component of phase A the absorbing phase. These two minerals are typical constituents of hard rocks.

At typical pressure levels quartz transforms from trigonal quartz (α -quartz) to hexagonal quartz (β -quartz) at 573 °C (Le Chatelier, 1889). The phase transition is accompanied by a change in symmetry and volume, where the β -quartz has higher symmetry and volume than the α -quartz (Moss, 1999). In order to consider the α to β phase transformation of quartz in the numerical model, material data in a range from room temperature up to about 800 °C is required. The elastic data as well as heat capacity and thermal expansion are taken from Carpenter et al. (1998). Their measurements of the lattice parameters form the basis for the calculation

Table 1

Temperature dependent thermo-mechanical properties of plagioclase. c_p = specific heat, k = thermal conductivity, α = thermal expansion coefficient, E = Young's modulus, v = Poisson's ratio and ρ = density.

Property (unit)	Temperature (°C)	Value	Source
c_p (J/kg K)	50	800	Benisek et al. (2013)
	200	945	
	400	1054	
	500	1090	
k (W/m K)	–	1.46	Horai and Baldridge (1972)
α (1/K)	25	$3.60 \cdot 10^{-6}$	Skinner (1966)
	119.85	$4.60 \cdot 10^{-6}$	
	219.85	$5.19 \cdot 10^{-6}$	
	319.85	$5.59 \cdot 10^{-6}$	
	419.85	$5.89 \cdot 10^{-6}$	
	519.85	$6.14 \cdot 10^{-6}$	
	619.85	$6.37 \cdot 10^{-6}$	
	719.85	$6.58 \cdot 10^{-6}$	
	819.85	$6.78 \cdot 10^{-6}$	
	919.85	$6.97 \cdot 10^{-6}$	
E (GPa)	–	87.02	Hearmon (1984)
	–	0.29	
v (1)	–	2703	Gebrände et al. (1982)
ρ (kg/m ³)	–	2703	Gebrände et al. (1982)

¹ For interpretation of color in Figs. 1, 5, 17 and 29, the reader is referred to the web version of this article.

of the transformation strains. Experimental data are compared in Carpenter et al. (1998) with theoretical curves obtained from a Landau-type modeling of the temperature dependence of strains and elastic moduli (Pitteri, 2013). The anisotropic thermal conductance is used from Gibert and Mainprice (2009) where the thermal diffusivity of single quartz crystals is measured by a modified Angström method up to a temperature of 800 °C.

In Sections 2.4.1–2.4.3 the thermo-mechanical properties of quartz are displayed as a function of temperature in order to gain a deeper understanding of the anisotropic behavior of quartz in a wide temperature range. The material response of plagioclase is assumed as isotropic and the material data is taken from literature. Table 1 illustrates the material properties of plagioclase used in this study.

2.4.1. Heat capacity and thermal conductance

The thermal material behavior of quartz is depicted in Figs. 6 and 7 in a range from room temperature up to 800 °C. The vertical line indicates the phase transformation temperature from α -quartz to β -quartz.

The heat capacity c_p is a scalar quantity and thus represented by just one line in Fig. 6. The hotter the quartz gets the more thermal energy is needed to further enhance the temperature. At the phase transformation significantly more energy (due to the latent heat) is needed to change the crystallographic system (peak in Fig. 6). In Fig. 7 the anisotropic behavior of the thermal conductance k as well as its isotropic equivalent mean is visualized. Only a slight change at the phase transformation is noted. However, significant differences of the thermal conductance along the a - and c -axis are observed especially for the α -quartz.

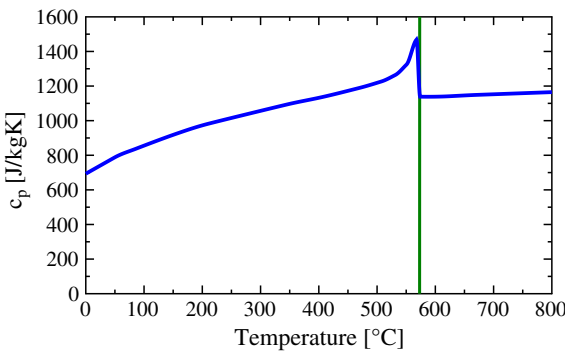


Fig. 6. Heat capacity c_p (J/kg K) as a function of temperature (°C) (Carpenter et al., 1998).

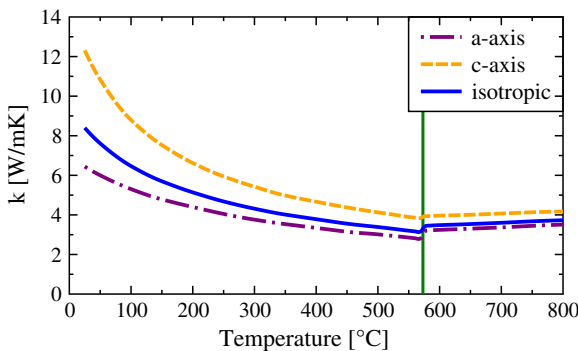


Fig. 7. Thermal conductance k (W/m K) in the isotropic and anisotropic case (Gibert and Mainprice, 2009).

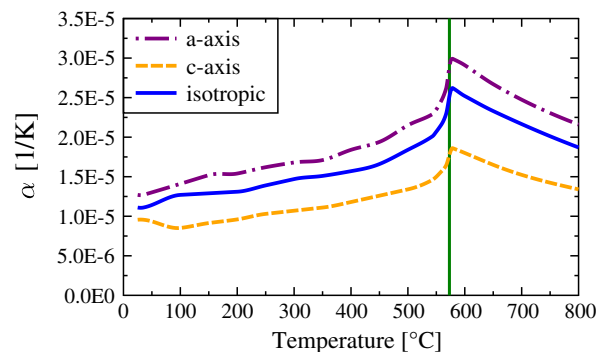


Fig. 8. Thermal expansion coefficient for the isotropic and anisotropic case (Carpenter et al., 1998).

2.4.2. Thermal expansion

Based on the thermal strains reported in Carpenter et al. (1998) the thermal expansion coefficient α with respect to a room temperature of 25 °C is derived (Fig. 8). The anisotropic thermal elongation of the quartz grains is also considered.

In Fig. 8 it is observed that the thermal expansion increases rapidly when the temperature is close to the phase transformation temperature. This is due to the jump of the density from the α to the β phase. In the β -quartz the thermal expansion coefficient α decreases since the thermal strains are nearly constant in this phase. Furthermore, a strong difference between the thermal expansion along the a -axis of the crystal and the c -axis is observed. This gives rise to the conjecture that strong anisotropic effects should be seen within the stress field of the anisotropic model.

2.4.3. Elastic constants

Based on symmetry considerations of the crystal structure in quartz seven elastic constants have to be defined in order to fully describe the elastic behavior. Actually, in the β phase only six constants are required since C_{14} is zero (Fig. 9), see Carpenter et al. (1998).

Fig. 9 shows the strong temperature dependence of the different elastic constants, especially near the α - β phase transformation. Furthermore, the crystal orientation suddenly changes at the phase transformation (e.g. C_{14} becomes zero in β -quartz and C_{11} the dominant coefficient). The isotropic material constants (Young's modulus E and Poisson number ν) are obtained analytically by means of a Voigt-Reuss-Hill averaging for the trigonal as well as hexagonal symmetry (Peselnick and Meister, 1965).

3. Results

The simulation methodology described in Section 2 is performed for three different numerical models with the same grain size and filling factor ($f = 0.34$) but different morphologies. The reference model (model A in Fig. 4) is further used to assess the influence of the phase transformation as well as the anisotropic behavior of the quartz grains (phase T). The results are organized in three main parts: FDTD-, thermal- and mechanical-results.

3.1. FDTD simulation

3.1.1. Electric field results of the reference model

Based on the outlined numerical model of a reference phase distribution the electric field inside the microstructure is determined. To this end the time averaged squared electric field (E^2) is evaluated after the 24th period, when the electric field has stabilized. This period has been found iteratively. In Fig. 10 the Euclidean

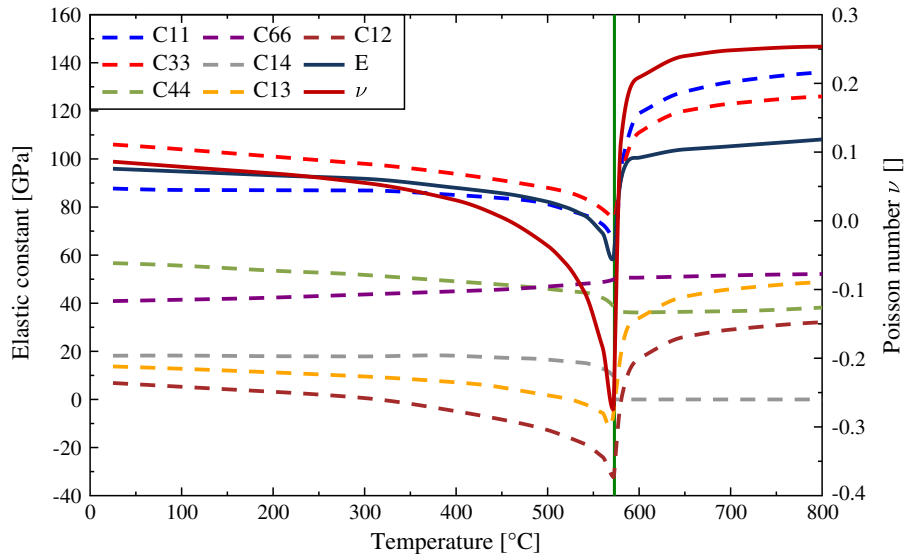


Fig. 9. Elastic constants (GPa) as a function of temperature (°C) (Carpenter et al., 1998). Isotropic elastic data is derived by a Voigt–Reuss–Hill averaging (Peselnick and Meister, 1965).

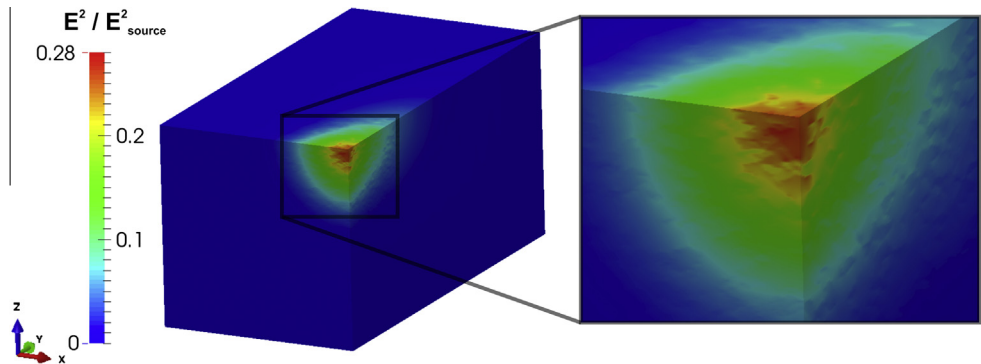


Fig. 10. Euclidean norm of the time averaged squared electric field E^2 scaled by the reference value at the center of the source position (E_{source}^2) in air.

norm of the E^2 field scaled by the reference value at the center point of the source (E_{source}^2) in air is illustrated.

By analyzing Fig. 10, a significant deviation from an ideal Gaussian beam, as it would appear in a homogeneous material, is observed. Furthermore, a stripe-like pattern occurs which would not be visible in the homogeneous case. Since the imaginary part of the effective permittivity is considerable, the microwave beam

does not penetrate deep into the material. Fig. 11 shows the difference between the inhomogeneous and homogeneous electric field at each point of the FDTD grid inside the material.

From Fig. 11 it can be seen that the electric field in the inhomogeneous model deviates quite significantly from the main beam in the homogeneous case. On average, however, the values of E^2 in the microstructure are slightly higher along the center of the

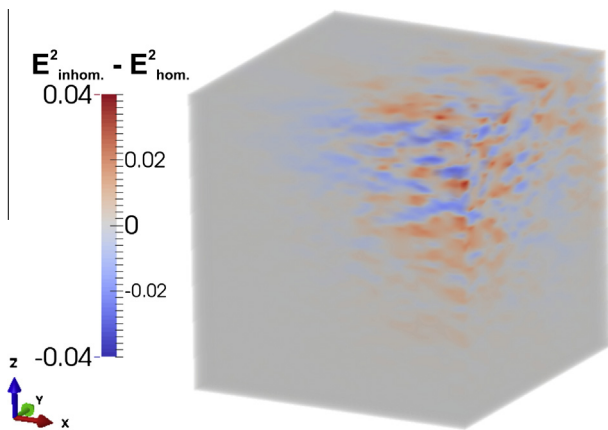


Fig. 11. Difference between the electric field of the inhomogeneous and the homogeneous model.

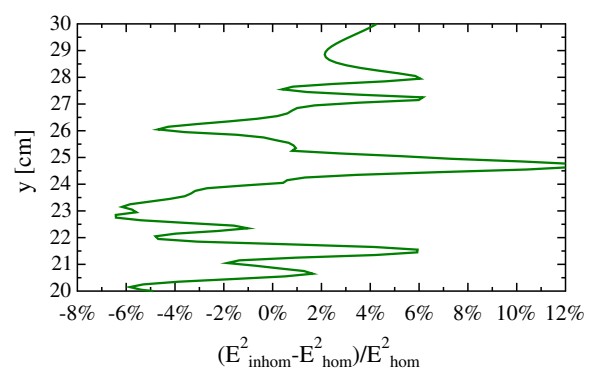


Fig. 12. Cut along the Gaussian axis ($x = 25 \text{ cm}, z = 25 \text{ cm}$) showing the relative difference of the inhomogeneous to the homogeneous model.

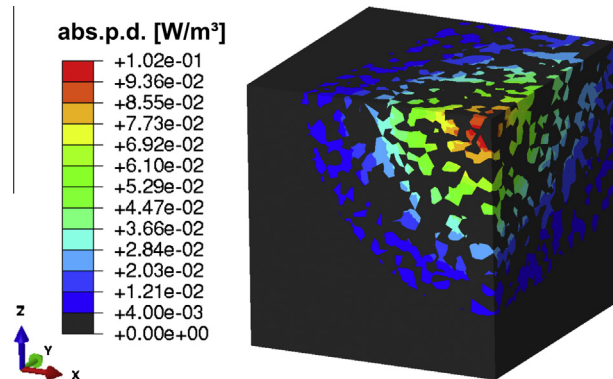


Fig. 13. Absorbed power density (abs.p.d.) in W/m^3 .

Gaussian beam as indicated by a cut along the middle axis of the Gaussian beam, “Gaussian axis” (in y -direction at $x=z=25 \text{ cm}$), see Fig. 12. A relative difference of up to 12% is observed. These deviations are caused by the differences of the real parts of the permittivity at the phase interfaces and by the non-zero imaginary part of phase A.

From the results of the FDTD analysis, the absorbed power density distribution can be worked out (Fig. 13), which serves as input for the subsequent FE simulations. According to the assumption that phase T is transparent for microwaves, absorption only occurs in phase A. As illustrated in Fig. 13 most of the energy is absorbed by few grains of phase A near the axis of the Gaussian beam.

3.2. Thermal simulation

3.2.1. Temperature field in the reference model

As described in Section 2.3 the body heat flux, which is derived from the absorbed power density, is applied at the integration points of each finite element through the subroutine DFLUX ([Abaqus, 2012](#)). Heating the reference model with a microwave source of 25 kW and assumed losses of 30% for 15 s results in a considerably inhomogeneous temperature field (Fig. 14).

In Fig. 14 a maximum temperature of 547 °C is observed in a depth of 1 cm along the axis of the Gaussian beam inside a phase A grain. Moreover, strong selective heating due to the selective absorption (see Fig. 13) combined with the variation of the thermal properties of the two constituents is obtained. The strong localization of areas with high temperatures leads to significant thermal gradients between the two material phases and therefore high thermal stresses are expected. However, the maximum temperature in phase T (quartz) is 482 °C, which is significantly below the α to β phase transformation temperature of 573 °C.

3.2.2. Temperature field in the case of a phase transformation

Since no α to β phase transformation in quartz has been observed in the reference model so far, a new model with the same morphology but 25 s irradiation time is considered. In Fig. 15 the temperature distribution of the 25 s model is compared with the one after 15 s of microwave irradiation.

By comparing the same microstructure model with 15 s and 25 s of irradiation time significantly higher temperatures in the 25 s model (maximum of 759 °C instead of 547 °C) are observed

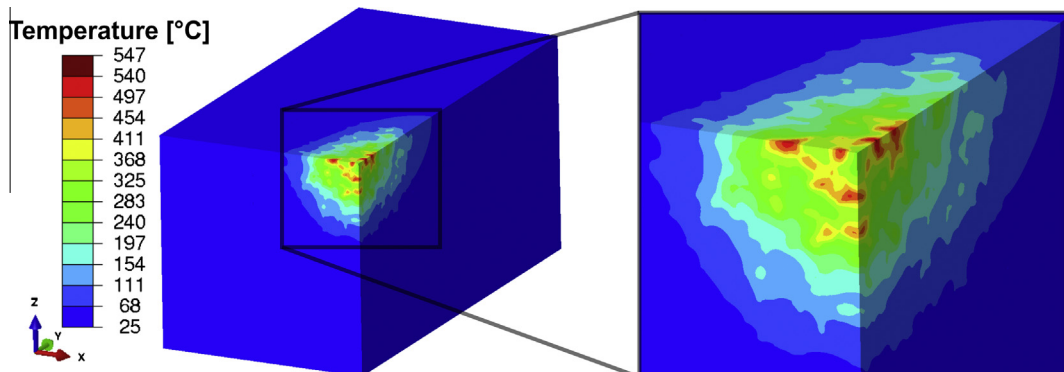


Fig. 14. Temperature field in °C after 15 s of microwave irradiation (25 kW minus 30% losses) of the reference morphology.

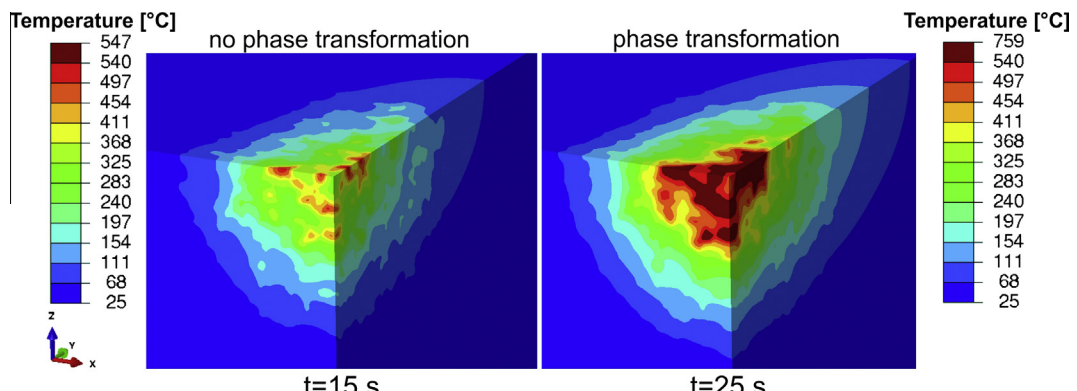


Fig. 15. Comparison of the temperature distribution in °C between 15 s and 25 s (incl. phase transformation) irradiation time.

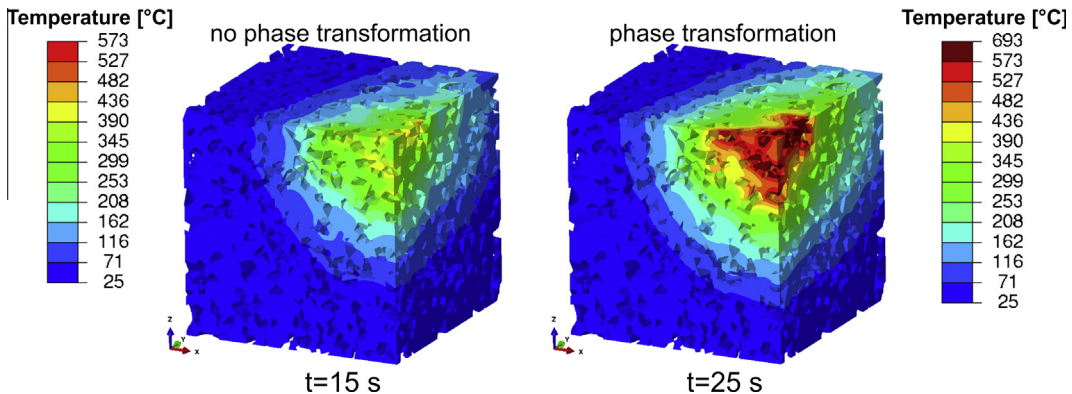


Fig. 16. Comparison of the phase T (quartz) temperatures in °C between the model of 15 s and 25 s microwave irradiation. The phase A elements are not displayed.

(Fig. 15). Furthermore, the depth and the radius of the area above 70 °C are larger due to the longer irradiation time. After 25 s of microwave heating a maximum temperature of 693 °C is observed inside phase T (quartz, Fig. 16). As a consequence the α quartz transforms to β quartz in areas near the hottest phase A grains around the Gaussian beam axis. For better visibility the phase A elements have been switched off in Fig. 16.

3.3. Mechanical simulation

Using the transient temperature field (obtained in Section 3.2) as an input and the boundary conditions described in Section 2.3, a stress analysis is conducted assuming an elastic material behavior of the two constituents. Since hard rocks can be considered as quasi-brittle, the maximum principal stress is an appropriate measure for assessing damage initiation. In order to compare the stress state with a material strength, an average tensile strength of hard rocks such as granite of 9 MPa (Hustrulid et al., 2001) is assumed as the strength limit. However, the strength of quartz and plagioclase minerals is slightly higher (Wang, 2015), the bulk strength limit was used since the phase boundaries are weaker than the minerals. The FE mesh equals the one of the thermal analysis and likewise uses elements with linear shape functions.

3.3.1. Stress field of the reference model

In the reference model high maximum principal stresses are observed in phase A grains near the front face of the rock model inside the main Gaussian beam (Fig. 17). There the stresses are significantly higher than the tensile strength of 9 MPa and therefore

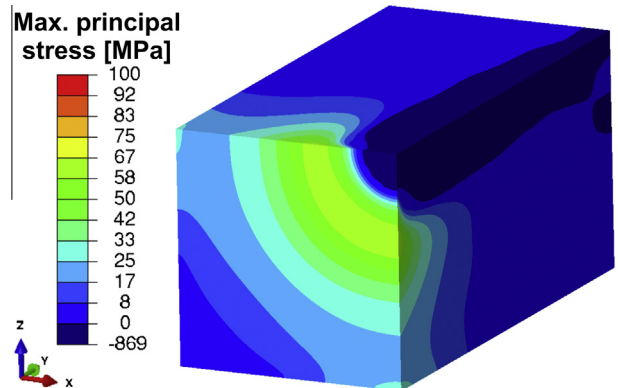


Fig. 18. Maximum principal stresses in MPa after 15 s of microwave heating of the homogeneous rock model.

damage initiation is expected. The tensile strength of 9 MPa is exceeded down to a depth of 10 cm (in direction of the microwave propagation) (light blue¹ areas in Fig. 17) indicating that initial surface cracks are likely to propagate in depth direction. After 4.2 s of microwave irradiation the maximum principal stresses at the phase boundaries and in small areas around the main irradiated spot already exceed the material strength.

In order to investigate the influence of the microstructure on the formation of the stress distribution, a comparative analysis including a homogeneous material definition is performed. By comparing Fig. 18 with the reference microstructure model

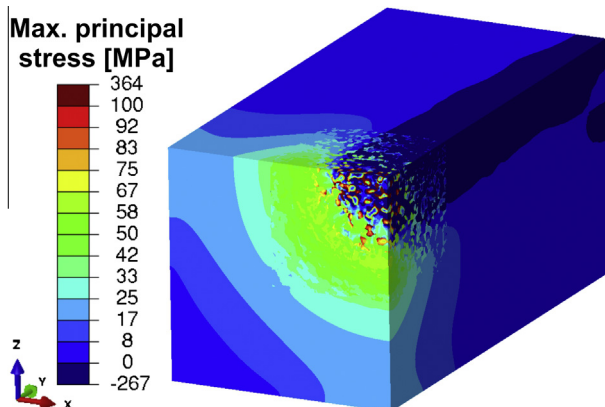


Fig. 17. Maximum principal stresses in MPa after 15 s of microwave heating of the inhomogeneous reference model.

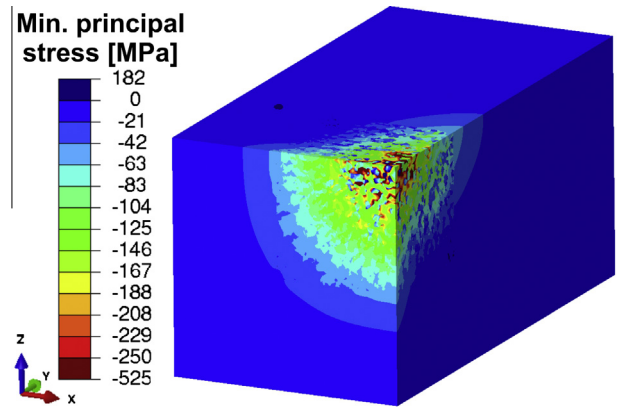


Fig. 19. Minimum principal stresses in MPa after 15 s of microwave heating of the reference morphology.

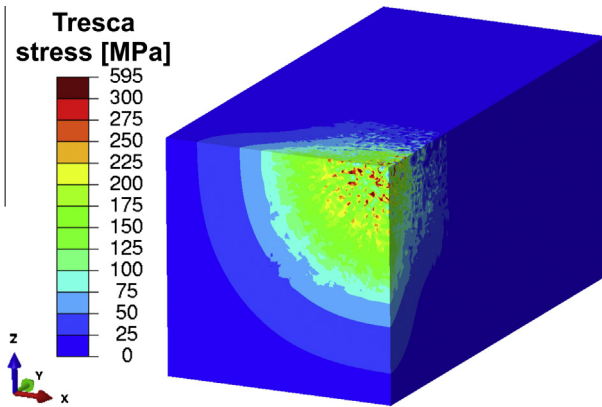


Fig. 20. Tresca stresses in MPa after 15 s of microwave heating of the reference morphology.

(Fig. 17) a significant deviation in the distribution of the stresses is determined. In the homogeneous case the highest principal stresses are observed around the main Gaussian beam (Fig. 18) whereas substantially higher stresses are found inside the main beam in phase A grains of the inhomogeneous model (Fig. 17).

In addition to brittle failure under tension, crushing due to compressive stresses has to be investigated. By comparing the minimum principal stresses (Fig. 19) with the compressive strength of hard rocks, which is about 250 MPa (Hustrulid et al., 2001), the areas of damage due to compression can be identified. In Fig. 19 it is visualized that the minimum principal stresses exceed the material limit in the vicinity of the Gaussian axis in the phase T grains near their phase boundaries.

The maximum principal stress is an appropriate measure as long as brittle behavior of the constituents is assumed. However, it has to be pointed out that in realistic rock materials different damage mechanisms might occur especially at elevated temperatures where non-negligible amounts of plasticity are to be expected. In that case an alternative failure criterion would allow more accurate predictions of the failure behavior of the rock. This is demonstrated on the example of the Tresca stress distribution function displayed in Fig. 20.

Tresca stresses exceeding the yield strength are observed in Fig. 20 in a broad area around the main irradiation spot. The highest values are located near the phase boundaries in both constituents close to the Gaussian axis. After 15 s of microwave irradiation plastic deformation is expected if ductile material behavior is assumed.

3.3.2. Stress results for different morphologies

By comparing the maximum principal stresses along the Gaussian axis of the three different morphologies (model A, B and C, see Fig. 4) with the homogenous model, the effects of the different phase assignments are assessed (Fig. 21). Moreover, a conjunction between temperature distribution (Fig. 22) and stress formation (Fig. 21) is drawn.

Considerable variations in the maximum principal stresses between the three models are observed (Fig. 21). Especially within the first centimeters of the material a strong deviation from the homogeneous model is determined. In model B and C significantly higher stresses than in the reference model (model A) are obtained. The influence of the microstructure on the selective heating of a rock and resulting formation of stresses due to microwave absorption is analyzed by illustrating the temperature profile along the Gaussian axis (Fig. 22).

In Fig. 22 a strong deviation of the temperatures of the inhomogeneous material models from the homogeneous one can be seen.

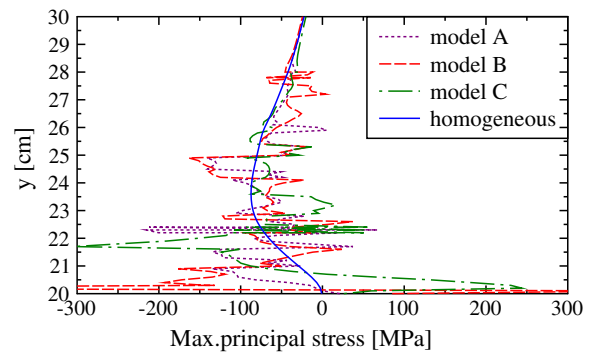


Fig. 21. Maximum principal stress profile along the y-direction of the Gaussian beam.

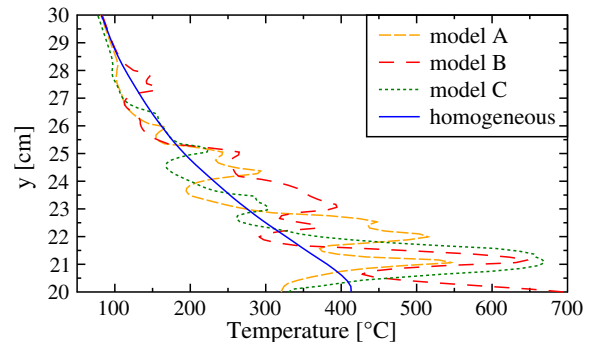


Fig. 22. Temperature profile along the y-direction of the Gaussian beam.

Furthermore, the strong thermal gradients are visualized which cause high thermal stresses. The largest deviation from the reference model A is observed in model B where the temperature near the surface is very high. This is due to a huge phase A grain on the front face at the beam axis (Fig. 4) which leads to a higher absorbed power and therefore higher temperatures (Fig. 22) and stresses (Fig. 21). Moreover, in model C higher temperatures than in model A occur.

3.3.3. Stress field after phase transformation

The influence of longer microwave irradiation times followed by α to β phase transformation of quartz is assessed by comparing the reference model with 15 s microwave treatment with a model with 25 s of microwave exposure (Fig. 23). Significantly higher maximum principal stresses are observed in phase A grains near the beam axis after 25 s of irradiation, see Fig. 23. Moreover a much larger area of high principal stress appears ($t = 25$ s). Also higher compressive stresses are formed in phase T as a consequence of the higher tensile stresses in phase A.

In order to investigate the influence of phase transformation and longer irradiation time in detail a statistical analysis of the stresses at the integration points of the finite elements located in the microstructure cube is performed. For that purpose the total stress range is divided into classes with a width of 1 MPa. A Python script loops over all integration-points and incrementally increases the frequency, expressed by the integration volume divided by total volume of the microstructure cube, of the class which the respective stress value belongs to. In Fig. 24 the frequency density distribution is plotted for the cases of 15 s as well as 25 s irradiation time, separately evaluated for both phases. The function values of the graph are derived by dividing the volume fraction in each class by the width of the class (Steland, 2013).

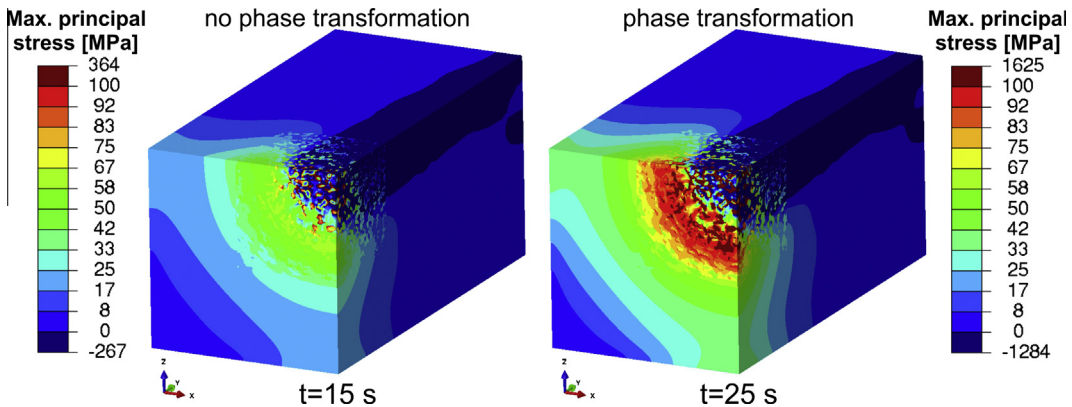


Fig. 23. Comparison of the maximum principal stresses in MPa between 15 s and 25 s (incl. phase transformation) irradiation time.

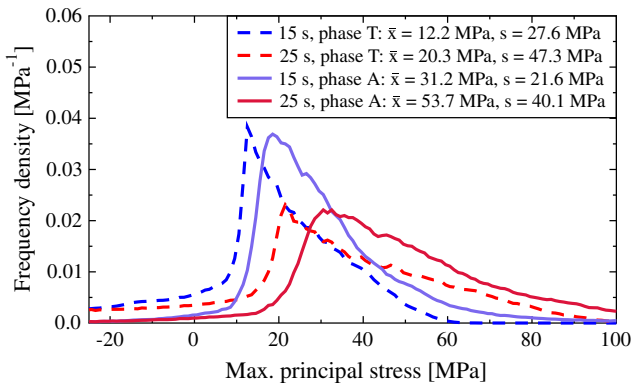


Fig. 24. Frequency density of the maximum principal stresses of phase T and phase A scaled to the respective volumes corresponding to the stress values. The legend includes the arithmetic mean \bar{x} as well as the standard deviation s .

In Fig. 24 a strong difference in the distribution of the maximum principal stresses between the model of 15 s and 25 s of microwave irradiation can be seen. In the 25 s case a significant shift of the frequency distribution to higher stresses for phase T (arithmetic mean of 20.3 MPa) as well as phase A ($\bar{x} = 53.7$ MPa) compared to the 15 s model (phase T $\bar{x} = 12.2$ MPa, phase A $\bar{x} = 31.2$ MPa) is observed. Moreover, a larger deviation between the phase T and phase A stress distribution in the model including phase transformation (25 s) occurs. However, the density distributions of the maximum principal stresses after 25 s of microwave irradiation are significantly broader (phase T $s = 47.3$ MPa,

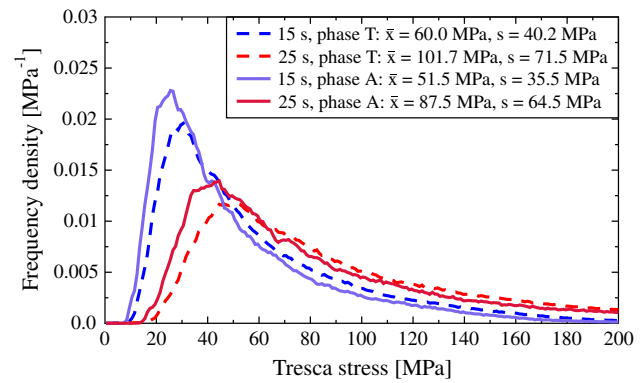


Fig. 26. Frequency density of the Tresca stresses of phase T and phase A scaled to the respective volumes corresponding to the stress values.

phase A $s = 40.1$ MPa) than in the 15 s case (phase T $s = 27.6$ MPa, phase A $s = 21.6$ MPa).

By visualizing the frequency density distribution of the minimum principal stresses (Fig. 25) a significant difference in the shape of the graphs compared to the maximum principal stresses (Fig. 24) is observed. Most of phase A are close to zero minimum principal stresses. Phase T contains significantly more volume with high compressive stresses than in phase A. Similar to the maximum principal stresses (Fig. 24) the curves are shifted to higher stresses in the 25 s irradiation case.

At elaborated stress levels the Tresca stress distribution of the both constituent is nearly coincident (Fig. 26). This is due to the fact that very high Tresca stresses are observed in phase T as well as in phase A near their boundary phases. A significant shift to higher stresses is observed after 25 s of microwave irradiation.

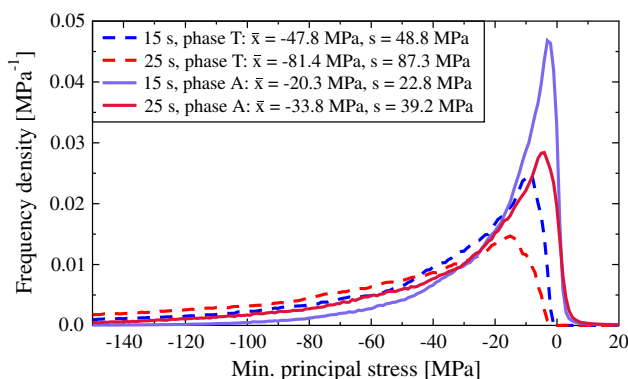


Fig. 25. Frequency density of the minimum principal stresses of phase T and phase A scaled to the respective volumes corresponding to the stress values.

3.3.4. Influence of anisotropic material behavior

The influence of the anisotropic behavior of the quartz grains (phase T) after 25 s of microwave heating of the reference model is investigated. To this end the stress distribution in the microstructure cube is calculated for both the isotropic as well as the anisotropic case (Fig. 27).

In Fig. 27 higher maximum principal stresses in phase A grains in a wider range than in the isotropic model are observed in the anisotropic model. Furthermore, due to the anisotropic behavior of the quartz grains tensile stresses occur in phase T (quartz) near the Gaussian beam that do not appear in the isotropic case. Especially near the Gaussian axis the quartz grains instantly change their orientation and elastic constants due to phase

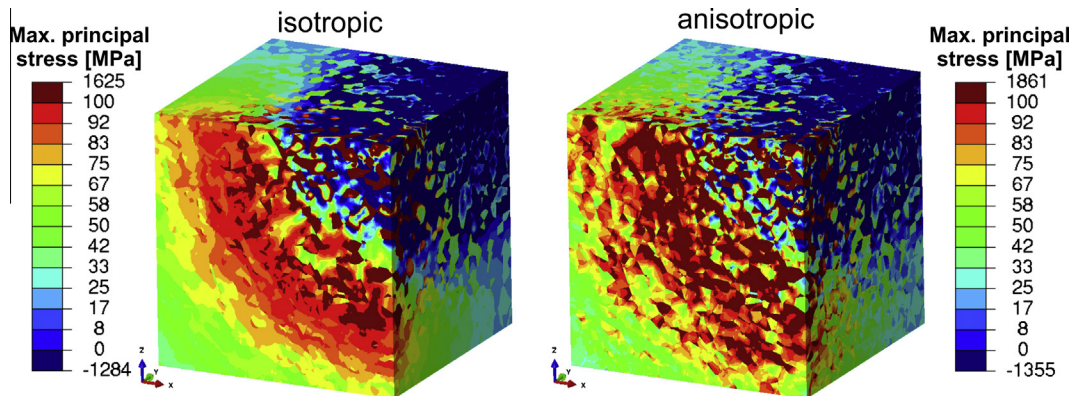


Fig. 27. Comparison of maximum principal stresses in MPa between the isotropic and anisotropic model after 25 s of microwave heating. Only cube containing the microstructure is visualized.

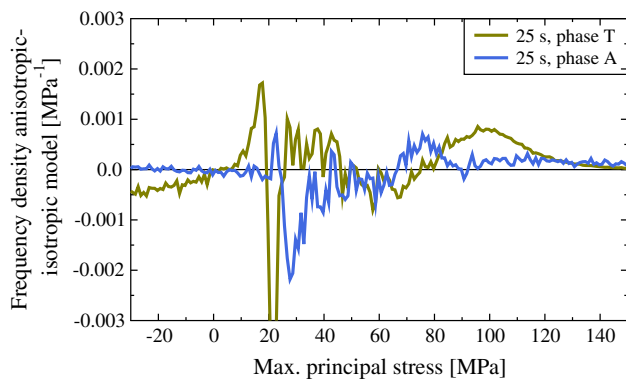


Fig. 28. Difference of the frequency density of the maximum principal stresses between the anisotropic and the isotropic model after 25 s of microwave irradiation.

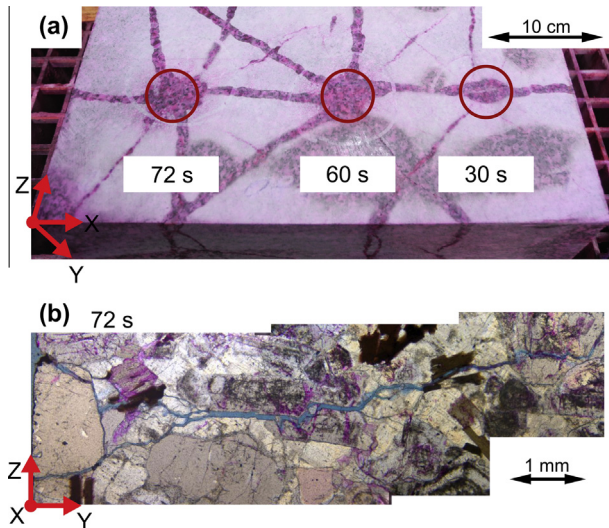


Fig. 29. Microwave irradiation with 25 kW (power of the microwave source) of granite for durations given in the figure. (a) Red circles indicating the area of highest intensity in the microwave beam. (b) Microstructure underneath hotspot of (a) after 72 s microwave irradiation. (For interpretation of the references to color in this figure legend, the reader is referred to the web version of this article.)

transformation. In addition higher temperatures are obtained in the anisotropic model which leads to higher thermal stresses. To investigate these differences in more detail a statistical analysis, as outlined in Section 3.3.3, is performed and the difference between the anisotropic and isotropic model is displayed (Fig. 28).

Fig. 28 reveals lower compressive stresses in phase T (quartz) and therefore higher tensile stresses up to a level of 20 MPa compared to the isotropic case. Furthermore, according to the anisotropic model in phase T significantly larger areas are subjected to stresses greater than 80 MPa. Moreover, a slightly higher fraction of phase A containing tensile stresses greater than 75 MPa is predicted by the model with anisotropic quartz behavior.

3.4. Experiments

Microwave irradiation experiments on granite blocks ($50 \times 50 \times 30 \text{ cm}^3$, 30 cm in direction of microwave irradiation) are performed using an open-ended rectangular waveguide ($4.3 \times 8.6 \text{ cm}^2$) as the applicator. Due to the few centimeters distance between waveguide and rock the area of the irradiated spot on the rock is approximately circular (red circle in Fig. 29a). The microwave source emits radiation with 25 kW at a frequency of 2.45 GHz. The power transmitted into the granite block is estimated to be 30% less. In Fig. 29 a first result of the experiments is illustrated for comparison with the results of the numerical analysis.

As illustrated in Fig. 29 intense cracking originating in a hot spot beneath the waveguide caused by the thermo-mechanical stresses is observed. Since the different irradiation spots are far apart from each other, only minor influences of the existing crack network on the crack initiation during the subsequent microwave irradiation experiment are assumed. By analyzing the in-depth crack paths into the material, see Fig. 29b, it is concluded that the microstructure has a major influence on the onset and subsequent accumulation of damage, since the cracks (blue¹ in Fig. 29b) mainly follow the grain boundaries. This implication agrees with the numerical results where the stress formation is driven by microstructural details.

4. Discussion

Regarding the effect of the microstructure on the microwave induced stresses in inhomogeneous rocks with strongly absorbing phases the stripe-like E² patterns are visualized in Fig. 10. In the vicinity of the microstructure/bulk material interface (Fig. 3) no artificial reflections are observed, which indicates that Bruggeman's effective medium theory works well in the current application. Moreover, there are only minor differences in the irradiation depth of the electric field between the homogeneous and the inhomogeneous model which also supports Bruggeman's formula. The further investigation of the difference between the inhomogeneous model and the homogeneous case (Fig. 11) shows a significant influence of the ϵ distribution within the microstructure model.

Along the axis of the Gaussian beam (Fig. 12) a deviation of 12% between the homogeneous and inhomogeneous model is visible. These deviations cause even more pronounced differences between the stress patterns in the inhomogeneous rock model as opposed to the homogeneous case. In the homogeneous model the highest maximum principal stresses occur around the main heated area (Fig. 18) whereas in the inhomogeneous case (Fig. 17) the boundaries of phase A grains near the Gaussian axis show the highest stresses. This implies a different damage mechanism for the two models. The question of whether crack formation can be induced by microwave heating is essentially dominated by the macroscopic thermal gradients. However, the position of damage initiation sites and the rates as well as propagation path will be influenced by the microstructure. Various studies performed with 2D microstructures containing absorbing particles in a non-absorbing matrix and constant microwave power densities concluded that the formation of damage depends on the microstructure (Ali and Bradshaw, 2010, 2011; Wang et al., 2008).

In the inhomogeneous case significant crack initiation is expected at the boundaries of the phase A grains near the Gaussian axis which will propagate along the phase boundaries in areas where high principal stresses occur as has been observed in the 2D case by Toifl et al. (2014). Additionally, high compressive stresses exceeding the material limit are identified at the phase boundaries in phase T (Fig. 19). For the homogeneous material the model predicts damage formation at the circumference of the Gaussian beam (Fig. 18). If elevated temperatures or high confining pressures are reached, a transition from brittle to ductile rock material behavior can occur. Under the assumption of ductile material behavior, plastic deformations arise near the phase boundaries of the inhomogeneous model due to high Tresca stresses (Fig. 20).

By comparing the stress field of three different morphologies with the same filling factor ($f = 0.34$, Fig. 21) the high influence of the microstructural details on the microwave induced stresses becomes evident. Although all three models feature equal averaged grain size ($d = 3.4$ mm), significant differences in the stress formation occur. Naturally, longer irradiation times lead to higher stresses. After 25 s of microwave irradiation phase transformation in the phase T (quartz) takes place which entails yet again higher stresses (Fig. 23). By performing a statistical analysis a strong shift of the stresses in phase T and phase A to higher maximum principal stresses is observed (Fig. 24). Furthermore, broader frequency density distributions of the maximum principal stresses in phase T and phase A are observed. A significantly higher portion of the irradiated volume contains stress values higher than 50 MPa after 25 s of microwave heating. Therefore a higher degree of damage is expected after 25 s of irradiation. Furthermore, there is also a shift to higher stresses in the graphs of the Tresca as well as minimum principal stress distributions.

The stresses increase if the anisotropic nature of the quartz crystals is taken into account. By comparing the stress field after 25 s of irradiation in the isotropic with those of the anisotropic case (Fig. 27) significantly more regions of high maximum principal stresses are observed in the anisotropic model. Furthermore, a statistical analysis of the stress formation in the isotropic as well as the anisotropic case (Fig. 28) shows that the anisotropic model predicts significantly fewer elements under compression and more elements under tension in phase T. Hence it is concluded that in the anisotropic model higher crack propagation dynamics is expected since the phase T grains do not have the potential to arrest a crack due to the lack of compressive stresses in the grains.

The set of stress results presented in Section 3.3 indicates that the consideration of the microstructural details is crucial to determine reliable microwave induced stresses in rocks with strongly absorbing phases. Moreover, different models with varying phase distributions but constant filling factors should be performed in

order to reveal statistically proven stress fields. Obviously, for an accurate prediction of the stress formation the phase transformation of quartz as well as the anisotropic nature has to be taken into account. These implications from the numerical analysis are supported by experimental investigations performed on granite blocks. Nevertheless, in future research a nonlinear damage constitutive law has to be implemented in the model in order to assess the microwave induced damage initiation and propagation. With this model the effect of the microstructural details on the formation of damage can be assessed. Furthermore, such a model allows comparing the damage behavior between the homogeneous and the inhomogeneous model.

5. Conclusion

A novel comprehensive 3D simulation chain for determining the microwave induced stresses in realistic microstructures has been presented. The concept comprises the analysis of the electric, the thermal and the stress fields of a two-component microstructure in a block of a model rock irradiated with a microwave beam. In order to apply the derived numerical methodology a model with thermo-physical properties taken from literature was built up. After 15 s of microwave irradiation the resulting maximum principal stresses exceed the material strength in a wide range. The highest stresses are observed at the boundaries of the absorbing phase near the Gaussian axis of the beam. Likewise, high stress concentrations near the phase boundaries are determined at the minimum principal as well as Tresca stress field. The stress history of the current model rock indicates that with the given conditions an irradiation time of 4.2 s could be enough to initiate local damage. However, a deeper analysis including damage models are needed to determine boundaries for the microwave irradiation time.

Comparing the maximum principal stress field of the inhomogeneous model with the homogeneous one reveals substantial differences. Obviously microwave induced stresses in materials with strongly absorbing phases depend on the microstructure. Sufficiently strong heating triggers a phase transformation in the quartz grains which leads to even higher stresses in both constituents. The stress state significantly changes when the anisotropic material behavior of quartz is taken into account. Then the quartz grains near the Gaussian axis, which were subject to strong compression in the isotropic case, change to tension in the anisotropic model. Therefore a different crack pattern is expected in the anisotropic case. The phase transformations as well as the anisotropic behavior of quartz crystals have the potential to promote damage in rocks with high amounts of quartz (i.e. granite, quartzolite, rhyolite, dacite). In future work not only damage initiation but also crack propagation will be modeled.

The presented simulation chain allows assessing different grain diameters, morphologies, constituents and filling factors. Moreover, the methodology can easily be extended to more than two constituents as well as an actual microstructure as measured by crystallographic investigations. For further investigations a more realistic grain size distribution including a spatial correlation will be taken into account. So far the reported methodology is limited to temperature independent dielectric properties since no strong coupling between FDTD and FE simulation has been considered. Future work will also include this effect in a more sophisticated simulation procedure. Moreover, a comprehensive measurement setup has to be devised in order to correlate the numerical models with the microwave experiments quantitatively. Afterwards, a general conclusion on the improvement of comminution efficiency due to microwave irradiation of hard rocks can be drawn. Nevertheless, the presented 3D simulations confirm that microwave treatment has the potential to induce high stresses which can eventually lead to damage formation.

Acknowledgement

Financial support by the Austrian Science Fund (FWF): TRP 284-N30 is gratefully acknowledged.

References

- Abaqus, 2012. Abaqus v6.12 Documentation. Providence, RI, USA: Dassault Systèmes Simulia Corp. <<http://www.3ds.com/products-services/simulia/products/abaqus/>>.
- Ali, A.Y., Bradshaw, S.M., 2010. Bonded-particle modelling of microwave-induced damage in ore particles. Miner. Eng. 23, 780–790. <http://dx.doi.org/10.1016/j.mine.2010.05.019>.
- Ali, A.Y., Bradshaw, S.M., 2011. Confined particle bed breakage of microwave treated and untreated ores. Miner. Eng. 24, 1625–1630. <http://dx.doi.org/10.1016/j.mine.2011.08.020>.
- Benisek, A., Dachs, E., Carpenter, M.A., 2013. Heat capacity and entropy of low structural state plagioclases. Phys. Chem. Miner. 40 (2), 167–173. <http://dx.doi.org/10.1007/s00269-012-0556-2>.
- Bruggeman, D.A.G., 1935. Berechnung verschiedener physikalischer Konstanten von heterogenen Substanzen. I. Dielektrizitätskonstanten und Leitfähigkeiten der Mischkörper aus isotropen Substanzen. Ann. Phys. 416 (7), 636–664. <http://dx.doi.org/10.1002/andp.19354160705>.
- Carpenter, M.A., Salje, E.K.H., Graeme-Barber, A., Wruck, B., Dove, M.T., Knight, K.S., 1998. Calibration of excess thermodynamic properties and elastic constant variations associated with the alpha – beta phase transition in quartz. Am. Mineral. 83, 2–22.
- Church, R.H., Webb, W.E., Salsman, J.B., 1988. Dielectric properties of low-loss minerals. Report of Investigations 9194, Bureau of Mines.
- Ciuchi, I.V., Olariu, C.S., Mitoseriu, L., 2013. Determination of bone mineral volume fraction using impedance analysis and Bruggeman model. Mater. Sci. Eng., B 178, 1296–1302. <http://dx.doi.org/10.1016/j.mseb.2013.04.001>.
- DOE, 2007. Mining industry energy bandwidth study. <http://www1.eere.energy.gov/manufacturing/resources/mining/pdfs/mining_bandwidth.pdf>.
- Fitzgibbon, K., Veasey, T., 1990. Thermally assisted liberation – a review. Miner. Eng. 3 (1–2), 181–185. [http://dx.doi.org/10.1016/0892-6875\(90\)90090-X](http://dx.doi.org/10.1016/0892-6875(90)90090-X).
- Fuerstenau, D.W., Abouzeid, A.-Z.M., 2002. The energy efficiency of ball milling in comminution. Int. J. Miner. Process. 67 (1–4), 161–185. [http://dx.doi.org/10.1016/S0301-7516\(02\)00039-X](http://dx.doi.org/10.1016/S0301-7516(02)00039-X).
- Gebrände, H., Kern, H., Rummel, F., 1982. Elasticity and inelasticity. In: Angenheister, G. (Ed.), SpringerMaterials – The Landolt-Börnstein Database: Physical Properties of Rocks. Springer-Verlag, Berlin, pp. 1–233.
- Gibert, B., Mainprice, D., 2009. Effect of crystal preferred orientations on the thermal diffusivity of quartz polycrystalline aggregates at high temperature. Tectonophysics 465 (1–4), 150–163. <http://dx.doi.org/10.1016/j.tecto.2008.11.006>.
- Hartlieb, P., Leindl, M., Kuchar, F., Antretter, T., Moser, P., 2012. Damage of basalt induced by microwave irradiation: Special Issue – Physical Separation. Miner. Eng. 31, 82–89. <http://dx.doi.org/10.1016/j.mine.2012.01.011>.
- Harmon, R.F.S., 1984. The elastic constants of crystals and other anisotropic materials. In: Hellwege, K.H., Hellwege, A.M. (Eds.), Landolt-Börnstein Tables, III/18. Springer-Verlag, Berlin, pp. 1–154.
- Horai, K., Baldridge, S., 1972. Thermal conductivity of nineteen igneous rocks, I application of the needle probe method to the measurement of the thermal conductivity of rock. Phys. Earth Planet. Inter. 5, 151–156. [http://dx.doi.org/10.1016/0031-9201\(72\)90084-2](http://dx.doi.org/10.1016/0031-9201(72)90084-2).
- Hustrulid, W.A., McCarter, M.K., Zyl, Van, Dirk, J.A., 2001. Slope Stability in Surface Mining. Society for Mining, Metallurgy & Exploration, Incorporated, Littleton.
- Jackson, J.D., 2011. Klassische Elektrodynamik. de Gruyter, Berlin.
- Jones, D.A., Kingman, S.W., Whittles, D.N., Lowndes, I.S., 2005. Understanding microwave assisted breakage. Miner. Eng. 18 (7), 659–669. <http://dx.doi.org/10.1016/j.mine.2004.10.011>.
- Kärkkäinen, K.K., Sihvola, A.H., Nikoskinen, K.I., 2000. Effective permittivity of mixtures: numerical validation by the FDTD method. IEEE Trans. Geosci. Remote Sens. 38 (3), 1303–1308.
- Křžmánc, M.M., Valant, M., Suvorov, D., 2003. The dielectric properties of plagioclase feldspars. Materiali tehnologije 37 (1–2), 13–17.
- Kogelník, H., Li, T., 1966. Laser beams and resonators. Appl. Opt. 5 (10), 1550–1567.
- Le Chatelier, H., 1889. Sur la dilatation du quartz. Comptes Rendus de l'Académie des Sciences de Paris 108, 1046–1049.
- Lou, J., Hatton, T.A., Laibinis, P.E., 1997. Effective dielectric properties of solvent mixtures at microwave frequencies. J. Phys. Chem. A 101, 5262–5268.
- Meisels, R., Toifl, M., Hartlieb, P., Kuchar, F., Antretter, T., 2015. Microwave propagation and absorption and its thermo-mechanical consequences in heterogeneous rocks. Int. J. Miner. Process. 135, 40–51. <http://dx.doi.org/10.1016/j.minpro.2015.01.003>.
- Moss, G.W., 1999. Mathematical models of the alpha-beta phase transition of quartz (Dissertation). Virginia Polytechnic Institute and State University, Blacksburg, Virginia, USA. <<http://scholar.lib.vt.edu/theses/available/etd-081099-142433/unrestricted/etd.pdf>>.
- Oskooi, A.F., Roundy, D., Ibanescu, M., Bermel, P., Joannopoulos, J., Johnson, S.G., 2010. Meep: A flexible free-software package for electromagnetic simulations by the FDTD method. Comput. Phys. Commun. 181 (3), 687–702. <http://dx.doi.org/10.1016/j.cpc.2009.11.008>.
- Oskooi, A., Johnson, S.G., 2011. Distinguishing correct from incorrect PML proposals and a corrected unsplit PML for anisotropic, dispersive media. J. Comput. Phys. 230 (7), 2369–2377. <http://dx.doi.org/10.1016/j.jcp.2011.01.006>.
- Peinsitt, T., Kuchar, F., Hartlieb, P., Moser, P., Kargl, H., Restner, U., 2010. Microwave heating of dry and water saturated basalt, granite and sandstone. Int. J. Mining Mineral Eng. 2 (1), 18–29. <http://dx.doi.org/10.1504/IJMME.2010.031810>.
- Peselnick, L., Meister, R., 1965. Variational method of determining effective moduli of polycrystals: (A) Hexagonal symmetry, (B) Trigonal symmetry. J. Appl. Phys. 36 (9), 2879. <http://dx.doi.org/10.1063/1.1714589>.
- Pitteri, M., 2013. On the elasticities of quartz across the - phase transformation. Math. Mech. Solids. <http://dx.doi.org/10.1177/1081286513501105>.
- Quey, R., Dawson, P., Barbe, F., 2011. Large-scale 3D random polycrystals for the finite element method: Generation, meshing and remeshing. Comput. Methods Appl. Mech. Eng. 200 (17–20), 1729–1745. <http://dx.doi.org/10.1016/j.cma.2011.01.002>.
- Santamarina, J.C. (Ed.), 1989. Rock Excavation with Microwaves: a Literature Review. Foundation Engineering: Current Principles and Practices. Publ by ASCE, Evanston, IL, USA.
- Satish, H., Ouellet, J., Raghavan, V., Radziszewski, P., 2006. Investigating microwave assisted rock breakage for possible space mining applications. Mining Technol. 115 (1), 34–40. <http://dx.doi.org/10.1179/174328606X101902>.
- Sihvola, A.H., 1989. Self-consistency aspects of dielectric mixing theories. IEEE Trans. Geosci. Remote Sens. 27 (4), 403–415.
- Skinner, B.J., 1966. Section 6: thermal expansion. Handbook of Physical Constants. Vol. 97 of Geological Society of America Memoirs. Geological Society of America, pp. 75–96.
- Steland, A., 2013. Basiswissen Statistik. Springer Spektrum, Berlin Heidelberg, Germany.
- Taflove, A., 1988. Review of the formulation and applications of the finite-difference time-domain method for numerical modeling of electromagnetic wave interactions with arbitrary structures. Wave Motion 10, 547–582.
- Taflove, A., 1995. Computational Electrodynamics: the Finite-difference Time-Domain Method. Artech House, Boston, London.
- Taflove, A., Oskooi, A., Johnson, S.G., 2013. Advances in FDTD computational electrodynamics: Photonics and nanotechnology. Artech House, Boston, London.
- Tang, X.W., Yang, X.B., Zhou, Y.D., 2014. An efficient algorithm for spatially-correlated random fields generation and its applications on the two-phase material. Solid State Commun. 182, 30–33. <http://dx.doi.org/10.1016/j.ssc.2013.12.009>.
- Toifl, M., Meisels, R., Hartlieb, P., Kuchar, F., Antretter, T., 2014. Microwave Absorption and its Thermo-mechanical Consequences in Heterogeneous Rocks. In: Soga, K., Kumar, K., Biscontini, G., Kuo, M. (Eds.), Geomechanics from Micro to Macro. Crc Press, pp. 1545–1550. <http://dx.doi.org/10.1201/b17395-281>.
- Tromans, D., 2008. Mineral comminution: Energy efficiency considerations. Miner. Eng. 21 (8), 613–620. <http://dx.doi.org/10.1016/j.mine.2007.12.003>.
- Wang, G., Radziszewski, P., Ouellet, J., 2008. Particle modeling simulation of thermal effects on ore breakage. Comput. Mater. Sci. 43, 892–901. <http://dx.doi.org/10.1016/j.commatsci.2008.02.005>.
- Wang, Y., Djordjevic, N., 2014. Thermal stress FEM analysis of rock with microwave energy. Int. J. Miner. Process. 130, 74–81. <http://dx.doi.org/10.1016/j.minpro.2014.05.012>.
- Wang, Y., 2015. Numerical modelling of heterogeneous rock breakage behaviour based on texture images. Miner. Eng. 74, 130–141. <http://dx.doi.org/10.1016/j.mine.2014.12.030>.
- Webb, W.E., Church, R.H., 1986. Measurement of dielectric properties of minerals at microwave frequencies, Report of Investigations 9035, Bureau of Mines.
- Yee, K.S., 1966. Numerical solution of initial boundary value problems involving Maxwell's equations in isotropic media. IEEE Trans. Antennas Propag. 14, 302–307.
- Zheng, Y., Wang, S., Feng, J., Ouyang, Z., Li, X., 2005. Measurement of the complex permittivity of dry rocks and minerals: application of polythene dilution method and Lichtenegger's mixture formulae. Geophys. J. Int. 163, 1195–1202. <http://dx.doi.org/10.1111/j.1365-246X.2005.02718.x>.
- Zhou, W., Hinojosa, B.B., Nino, J.C., 2012. Applicability of the Bruggeman equation for analyzing dielectric slurries containing ceramic powders with high permittivity. J. Am. Ceram. Soc. 95, 457–460. <http://dx.doi.org/10.1111/j.1551-2916.2011.05010.x>.